



## Direct numerical simulation of flow and acoustic fields around an air-reed instrument with tone holes

Hiroshi YOKOYAMA<sup>1</sup>, Masaki KOBAYASHI<sup>2</sup>, Hirofumi ONITSUKA<sup>3</sup>

Akira MIKI<sup>4</sup>, Akiyoshi IIDA<sup>5</sup>

<sup>1,2,5</sup> Toyohashi University of Technology, Japan

<sup>3,4</sup> Yamaha Corporation, Japan

### ABSTRACT

In order to clarify flow and acoustic fields around a recorder with opened and closed tone holes, direct aeroacoustics simulation was performed with compressible Navier-Stokes equations. For validation of the computational accuracy, the velocity distribution and sound pressure level were experimentally measured. The predicted velocity profile of jet ejecting from the windway is in good agreement with that of experiment. The numerical results show that the fundamental frequency and sound pressure level of predicted sound are almost the same as that of experiments. The path of the standing wave of the recorder was estimated with the pressure distribution. The open-end corrections found to be longer than those for a conventional simple pipe due to the effects of the impinging jet on the edge and the uniform flow in the resonator. When the vortices of the jet from the windway are getting near to the edge, strong deformation of the vortices occurs and expansion wave radiates in the resonator. The amplitude and phase of the acoustic particle velocity are almost the same as those of the jet itself. It indicates that the acoustic field amplifies the fluctuations of the jet and maintains the acoustic and fluid relations.

Keywords: Musical Instrument, Aeroacoustics, Acoustic-Fluid interactions  
I-INCE Classification of Subjects Number(s) : 26.1

### 1. INTRODUCTION

Since the sound quality of the music instruments depend on various factors, materials, shape and players skill, it is a very important experience of the craftsman in the development of the musical instruments. All players are seeking music instruments with good sound quality. It is therefore necessary to clarify scientifically generation mechanism of the sound of music instruments to establish a design method.

In air-reed instruments such as flutes, bamboo flutes, recorders and so on, fluid-acoustic interactions consisting of vortices and resonance in a pipe occurs [1]. Many researchers have been investigated these phenomena. Yoshikawa *et al.* [2] measured the flow field around the exit of the windway and mouth by using Particle Image Velocimetry (PIV) and identified the acoustic sources based on the Howe' vortex theory [3]. Giordano [4] investigated the effects of the chamfers of the windway exit and the position of the edge with reference to the windway on the tonal sound using the direct numerical simulations based on the Navier-Stokes equations, taking the ideal gas equation of state and assuming adiabatic conditions. However, the mechanism of the acoustic radiation and that of the generation of the vortices due to the acoustic feedback have not been clarified. Furthermore, the relationship between the pressure fluctuations of the standing wave in the pipe and the open-end corrections, which are used in the simple prediction of the acoustic resonant frequency of the pipe, has not been clarified.

---

<sup>1</sup> h-yokoyama@me.tut.ac.jp

<sup>2</sup> kobayashi@aero.me.tut.ac.jp

<sup>3</sup> hirofumi.onitsuka@music.yamaha.com

<sup>4</sup> akira.miki@music.yamaha.com

<sup>5</sup> iida@me.tut.ac.jp

To clarify the above-mentioned phenomena, the direct numerical simulations based on the compressible Navier-Stokes equations are performed for an actual recorder (YRA-28BIII) as shown in Figure 1. To validate the computational accuracy, the velocity field and sound pressure level are measured by PIV and microphone, respectively.

The sound wave receptivity of the jet oscillation around the edge is evaluated to compare order of fluctuation velocity and acoustic particle velocity. Moreover, the phase difference of pressure fluctuations in the resonant pipe is measured to find out the path of the standing wave and estimates the length of the open-end corrections of actual recorders. Moreover the effects of the jet velocity and the state of tone holes on sound generation of a recorder are investigated.

## 2. Computational Methodologies

### 2.1 Flow Conditions

The flow and acoustic fields around a recorder were investigated by using a short recorder with three tone holes as shown in Figure 1. In this paper, hereafter, this model is called as “full model”. For PIV measurements, one of the models was divided into half in the center of spanwise direction as shown in Figure 1(b). In this paper, hereafter, this model is called as “half model”. Each tone holes are called “Tone hole 0”, “Tone hole I” and “Tone hole II” in turn from that is near to a mouthpiece as shown in Figure 1.

Figure 2 shows schematics for configurations of recorder. The origin of coordinate system is located at the center of the outlet of the windway in the vertical and spanwise directions for the full model. For the half model, the origin is set at the boundary between the model and the acrylic board. The streamwise direction in the windway was the  $x$ -axis, the vertical direction was the  $y$ -axis, and the spanwise direction intersection with those two axes was the  $z$ -axis.

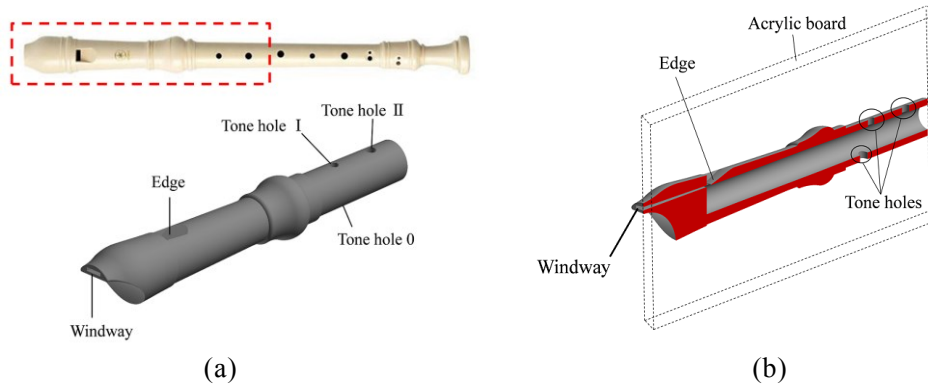


Figure 1 Computational models of recorder (YRA-28BIII). (a) Full model. (b) Half model.

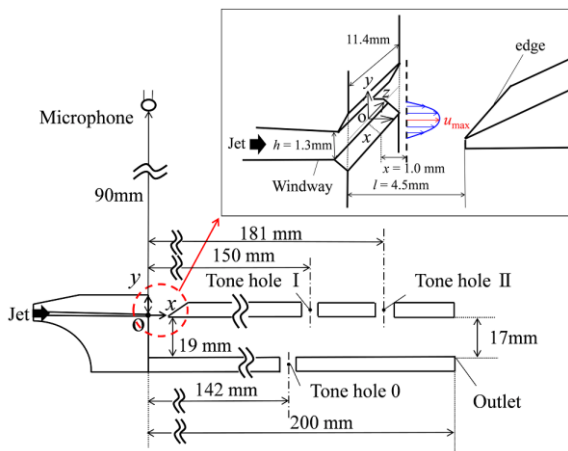


Figure 2 Configurations of recorder.

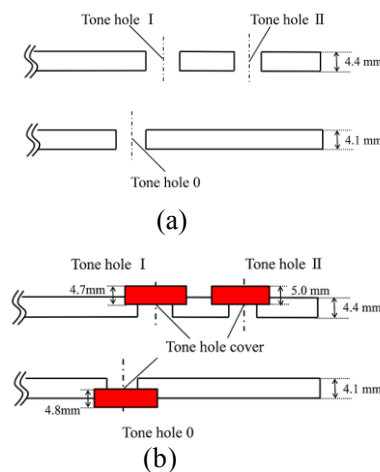


Figure 3 Opening and closing of tone holes. (a) With opened tone holes. (b) With closed tone holes

Table 1 shows experimental and numerical conditions of the recorder investigations. In order to estimate the effects of the flow rate on sound level and the frequency, the flow rate is changed from 7.1 L/min to 9.0 L/min in full model simulation and from 7 L/min to 30L/min in experiment. The flow rate of the half model for PIV measurement is set to  $Q = 3.55$  L/min. The jet velocities correspond to change from  $U_{\max} = 11.3$  to 13.7 m/s in the simulation, and from  $U_{\max} = 11.2$  to 40.2 m/s in experiment. The simulation velocities are the almost the same as the velocities of the actual velocity for musical performance,  $U_{\max} = 10 - 15$  m/s.

The flow and acoustic fields are measured with state of tone holes as parameters of sound quality of recorders.

Table 1 Condition for experiment and simulation of recorder

Model	Tone holes	Flow rate $Q$ [L/min]	Jet velocity $U_{\max}$ [m/s]	Mach number
Half model	Open	3.55 (Comp. and Exp.)	11.8	0.034
		7.1 (Comp.)	11.3	0.033
Full model	Open	9.0 (Comp.)	13.7	0.040
		7.0~35 (Exp.)	11.2 ~ 46.5	0.033 ~ 0.137
	Close	9.0 (Comp.)	13.7	0.040
		7.0~30 (Exp.)	11.2 ~ 40.2	0.033 ~ 0.118

## 2.2 Governing Equations and Finite Difference Formulation

In order to simulate the interactions between flow and acoustic fields, the three-dimensional compressible Navier-Stokes equation was directly solved using the sixth-order-accurate compact finite difference scheme (the forth-order-accurate at the boundaries) [5]. The time integration was performed using the third-order-accurate Runge-Kutta method. To reproduce the complex shape of the recorder on rectangle grid, the VP (Volume penalization) method [6] was utilized. The external force term, the penalization term  $V$ , is added to right hand side of the governing equations of the three-dimensional compressible Navier-Stokes equations as follows:

$$\mathcal{Q}_t + (E - E_v)_{x_1} + (F - F_v)_{x_2} + (G - G_v)_{x_3} = V \quad (1)$$

$$V = -(1/\phi - 1)\chi \begin{pmatrix} \partial \rho u_i / \partial x_i \\ 0 \\ 0 \\ 0 \\ 0 \end{pmatrix}, \quad (2)$$

$$\phi = 0.25, \quad (3)$$

$$\chi = \begin{cases} 1 & \text{(inside object)} \\ 0 & \text{(outside object)} \end{cases}, \quad (4)$$

where  $\mathcal{Q}_t$  is the vector of the conservative variables,  $E$ ,  $F$  and  $G$  are the inviscid flux vectors,  $E_v$ ,  $F_v$  and  $G_v$  are the viscous flux vectors,  $\phi$  is the porosity of porous medium,  $\chi$  is the mask function. The porosity  $\phi$  was determined so that the sound wave can be reflected almost completely (reflectivity : 99%).

In order to reduce the computational cost, large-eddy simulations (LES) were performed. No explicit SGS model was used. The turbulent energy in the GS that should be transferred to SGS eddies is dissipated by a 10th-order spatial filter of equation (5). The filter also suppresses the numerical instabilities associated with the central differencing in the compact scheme [7].

$$\alpha_f \hat{\psi}_{i-1} + \hat{\psi}_i + \alpha_f \hat{\psi}_{i+1} = \sum_{n=0}^5 \frac{a_n}{2} (\psi_{i+n} + \psi_{i-n}), \quad (5)$$

where  $\psi$  is a conservative quantity,  $\hat{\psi}$  is the filtered quantity. The coefficients  $a_n$  has the same value as those used by Gaitonde and Visbal [8], and the value of parameter  $\alpha_f$  is 0.45.

### 2.3 Computational Grid

Figure 4 shows the computational domain. The computational domain in the  $x$ - $y$  cross-section is divided into three regions; a vortex region, a sound region and a buffer region having different grid spacings. In the vortex region, the grid spacing is set to be fine the minimum to capture vortices around the edge and the shear layer as shown in Figure 5. The maximum spacing is  $\Delta f_{\min} = 0.05$  mm and corresponds to  $h/26$ , where  $h$  is the minimum windway height. The dominant vertical structures related to tones are approximately captured by 10-12 grid points. In the sound region, more than 10 grid points are used per fundamental wavelength. Also, in the buffer region, the grid is stretched to weaken acoustic wave near the artificial outflow boundary. The total grid points are approximately  $8.2 \times 10^7$  grid points.

### 2.4 Boundary Condition

Non-reflecting boundaries were used at boundaries of  $x$  and  $y$  directions as shown in Figure 4 and the periodic boundaries were used in the  $z$  direction. To reproduce the jet in the windway, the blowing was applied to the inlet region of the windway. The blowing velocity was shown in Figure 4.

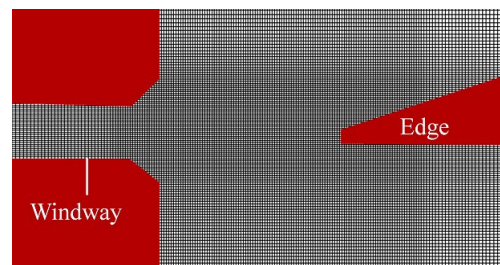
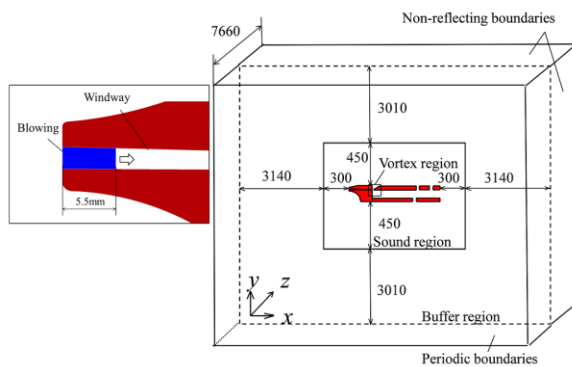


Figure 4 Computational domain and boundary condition.

Figure 5 Computational grid near windway and edge.

## 3. Validation of Computational Methods

### 3.1 Flow Fields

The predicted flow and acoustic fields were validated with comparison of those of measurements. Figure 6 shows the comparison of mean velocity profiles of numerical predictors and experiments at  $x/h = 0.22$ ,  $z/h = 0$ . The predicted profiles are in good agreement with those of measurements.

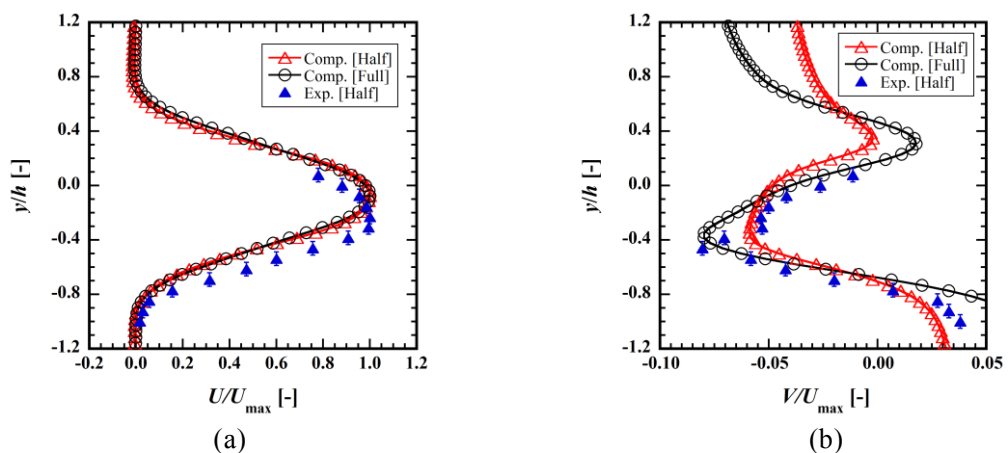


Figure 6 Mean velocity profiles ( $U_{\max} = 13.7$  m/s, open holes). (a) Streamwise velocity. (b) Normal velocity

### 3.2 Sound Pressure Level

Figure 7 shows the predicted and measured sound spectra with opened and closed holes at  $x = 0, y = 90, z = 0$ . The fundamental tone and overtones are reproduced and the predicted frequency and sound pressure level of fundamental tone are in agreement with those of measurement.

Moreover, Figure 8 shows the effect of the jet velocity  $U_{max}$  on the sound pressure level and Strouhal number ( $St \equiv f/U_{max}$ ) of the fundamental tone. As the velocity increases, the sound pressure level becomes intense, and the  $St$  decreases because of the resonance frequency of resonant pipe remains constant under flow condition is changed. The tendency of the sound pressure level and frequency change with the state of tone holes, closed and opened, agreed with the experiments and numerical simulations. It has been concluded that the present computational methods can adequately capture flow and acoustic field around the recorder.

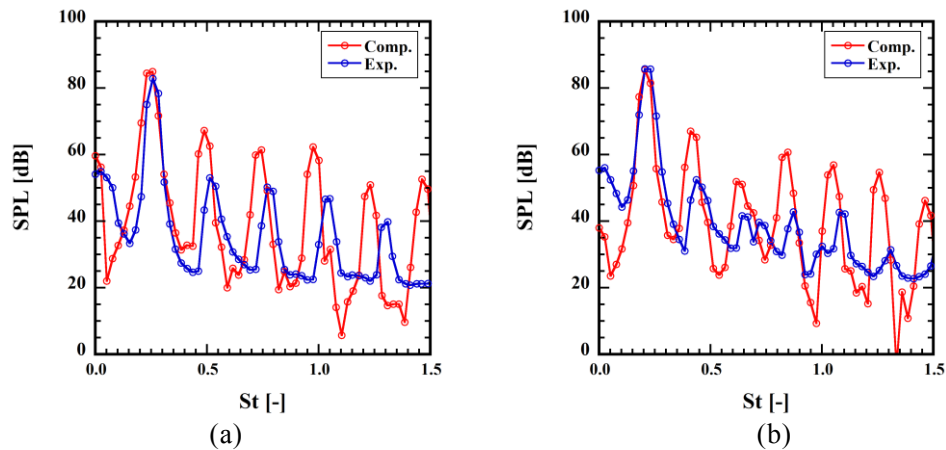


Figure 7 Comparison of predicted and measured sound spectra ( $U_{max} = 13.7$  m/s) (a) With opened holes. (b) With closed holes.

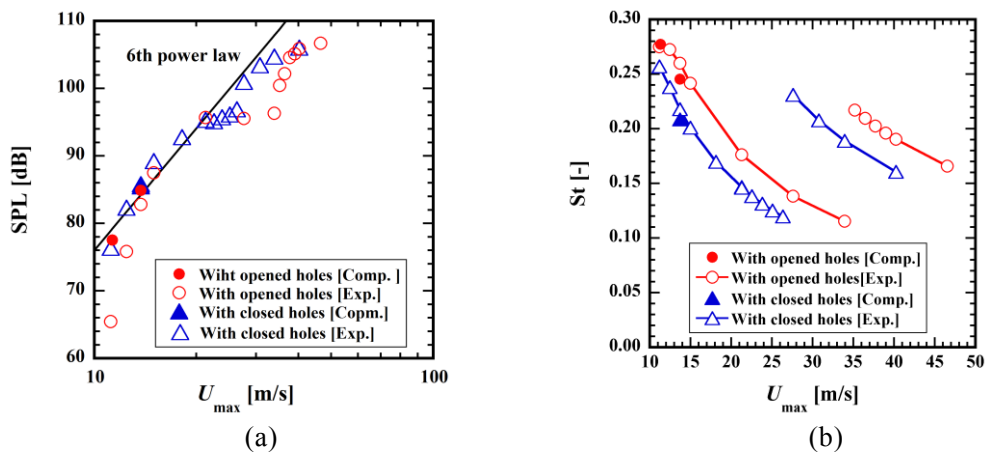


Figure 8 Dependency of jet velocity on sound pressure level and frequency of fundamental tone of a recorder. (a) Sound pressure level. (b) Fundamental frequency.

## 4. Result and Discussion

### 4.1 Fluid-Acoustic Interactions

#### 4.1.1 Acoustic Radiation

Figure 9(a) shows the fluctuation pressure  $p'$  around the recorder. Figure 9(b) shows the fluctuation pressure  $p'$  and vorticity  $\omega$  around the edge. Figure 9(c) shows the vorticity and the iso-surfaces of the second invariant of the velocity gradient as vertical structures. In these figures,  $T$  is the time period, of the fundamental frequency. The origin of time,  $t = 0$ , is defined as the fluctuation pressure became the maximum value on the center line of the resonator pipe.

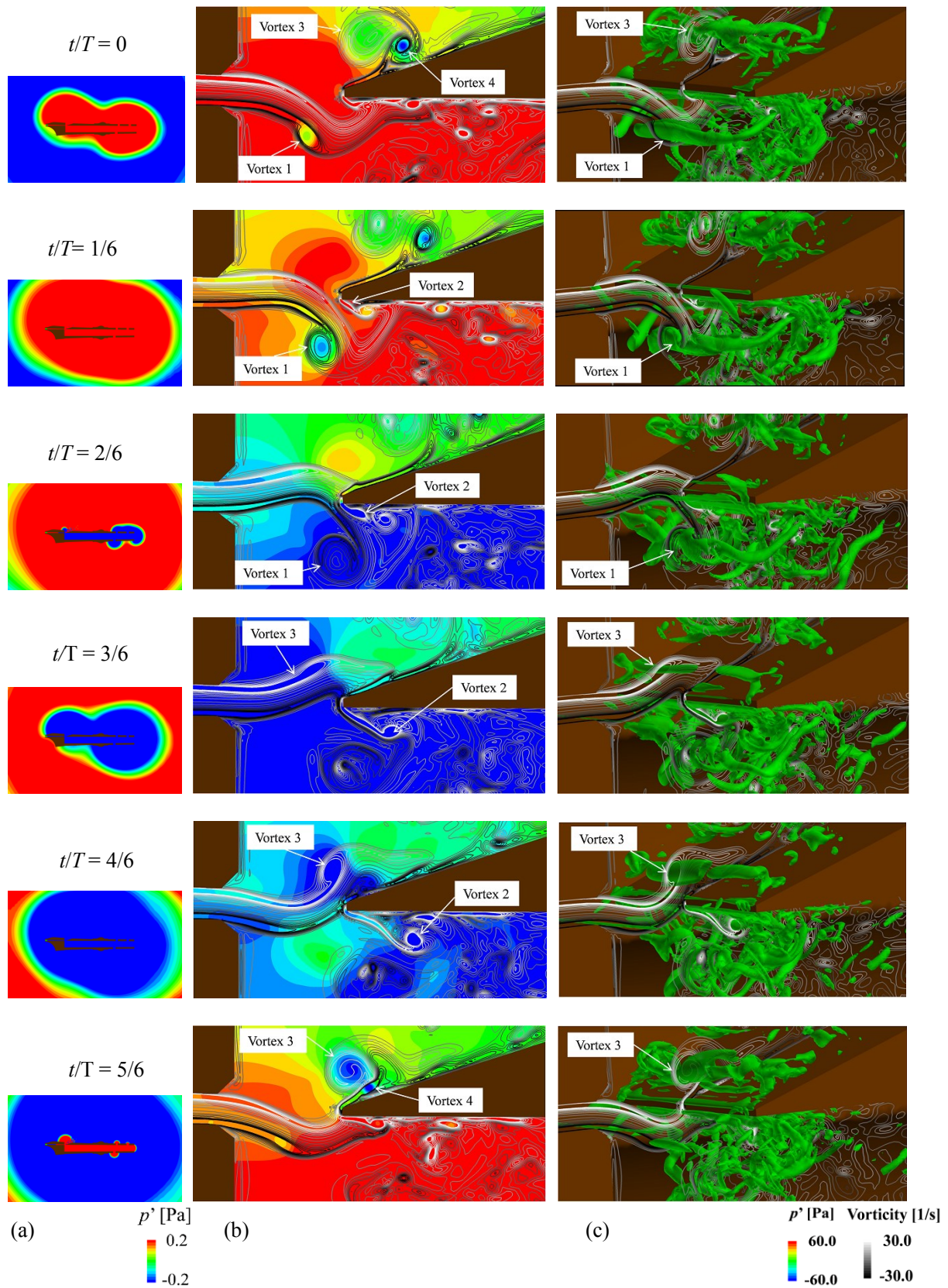


Figure 9 Time variation of flow and acoustic fields ( $U_{\max} = 13.7$  m/s, open holes). (a) Contours of fluctuation pressure (b) Contours of fluctuation pressure and vorticity (c) The iso-surfaces of the second invariant of the velocity gradient and contours of vorticity.

At  $t = 0$ , the two-dimensional vortex (Vortex 1) is formed in the free shear layer inclined downwards. At  $t/T = 1/6$ , Vortex 1 is moving with the negative pressure region and is getting close to the edge. At  $t/T = 2/6$ , Vortex 1 reaches the bottom of edge and the fluctuation pressure in the resonator pipe changes from the positive value to the negative value.

Figure 11 shows variation of the vorticity of the Vortex 1 with  $x/l$ . The vorticity rapidly decreases from  $t/T = 3/30$ . This decrease also occurs at  $U_{\max} = 11.3$  m/s. As a result, the balance between the centrifugal force and the pressure gradient collapses and the expansion were radiated.

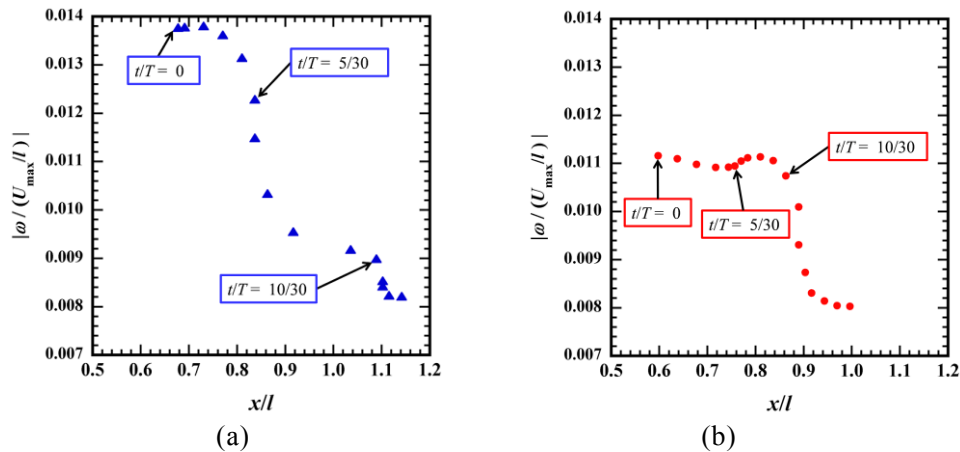


Figure 11 Variation of vorticity of Vortex 1 convecting in shear layer. (a)  $U_{\max} = 11.3$  m/s. (b)  $U_{\max} = 13.7$  m/s.

#### 4.1.2 Generation of Jet oscillation due to Feedback

Figure 12 shows the vectors of the fluctuation velocity  $V'$  ( $=V-V_{\text{ave}}$ ) and the contour of the fluctuation pressure around the edge at  $t/T = 8/30$  and  $t/T = 22/30$ . Direction of the fluctuation velocity at close to outlet of windway becomes upper at  $t/T = 8/30$  and downward at  $t/T = 22/30$ . The amplitude of velocity fluctuation,  $V_a' = 1.7$  m/s, at the point A ( $x/l = 0.22, y/h = -1.54, z/h = 0$ ) at  $t/T = 8/30$  approximately agrees with the theoretical acoustic particle velocity roughly estimated by the amplitude of acoustic pressure fluctuations of standing waves in the resonant pipe,  $V_a^{1'} (\equiv \rho c/p'_{\max}) = 2.1$  m/s, where  $p'_{\max}$  is the amplitude of the pressure fluctuation at the anti-node in the resonator. Therefore, these fluctuations represent the acoustic particle velocity.

Figure 13 shows the fluctuation velocity at the origin ( $x/l = 0, y/h = 0, z/h = 0$ ),  $V_f'$  for  $U_{\max} = 13.7$  m/s and those at point A,  $V_a'$  ( $x/l = 0.22, y/h = -1.54, z/h = 0$ ) for  $U_{\max} = 11.3, 13.7$  m/s with opened and closed holes. The amplitude and phase of the acoustic particle velocity are almost the same as the velocity fluctuation. This indicates that these oscillations of the free shear layer are induced by the acoustic feedback. Figure 13 (b) shows the velocity distributions along  $y = 0$  and  $z = 0$  at each time. It is shown that the disturbances induced by the acoustic feedback are convected downstream and developed to the vortices.

Figure 14 shows the fluctuation velocity at  $y/h = 0, z/h = 0$ . At  $t/T = 22/30$ , the negative velocity at  $x/l = 0.16$  indicates the downward in direction of the shear layer due to acoustic feedback. This disturbance is convected for the edge in the shear layer.

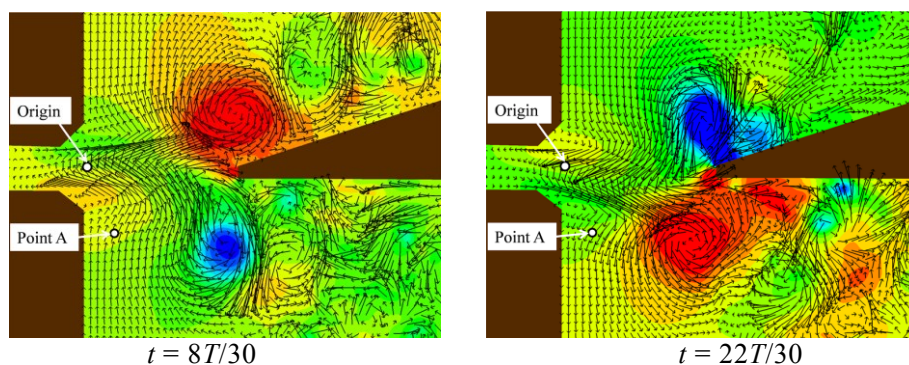


Figure 12 Contour of the fluctuation pressure and fluctuation velocity vectors near the edge.

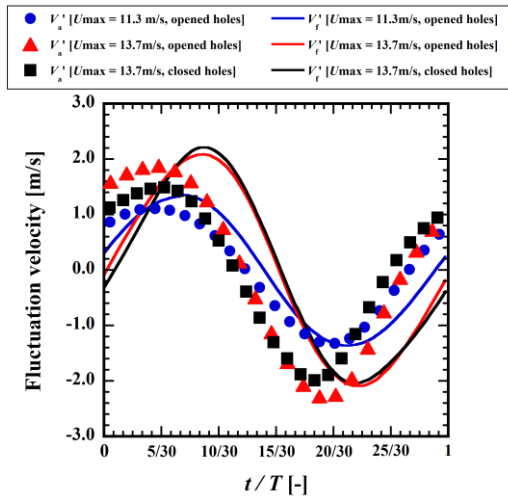


Figure 13 Velocity fluctuations of shear layer at the origin ( $x/l = 0, y/h = 0, z/h = 0$ ),  $V'_t$ , and those of acoustic particle velocity at point A ( $x/l = 0.22, y/h = -1.54, z/h = 0$ ),  $V'_a$ , for  $U_{max} = 11.3, 13.7$  m/s with opened and closed holes

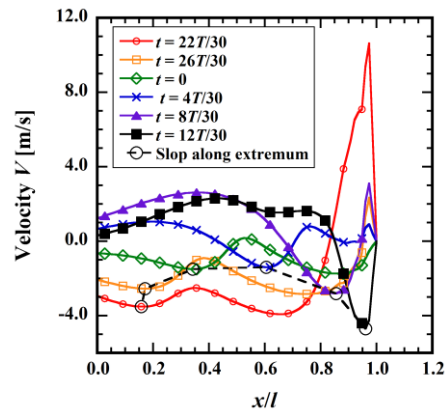


Figure 14 Convective acoustic particle velocity around edge ( $y/h = 0, z/h = 0$ )

## 4.2 Standing Waves in Resonant Pipe

### 4.2.1 Standing Waves

Figure 15 shows the contour of the fluctuation pressure for  $U_{max} = 13.7$  m/s at  $t/T = 0, 15/30$ . The standing wave can be observed in the resonator pipe of recorder. The positions of the antinode of the sound pressure are placed around 65 mm and 85 mm in the case of opened and closed tone holes, respectively.

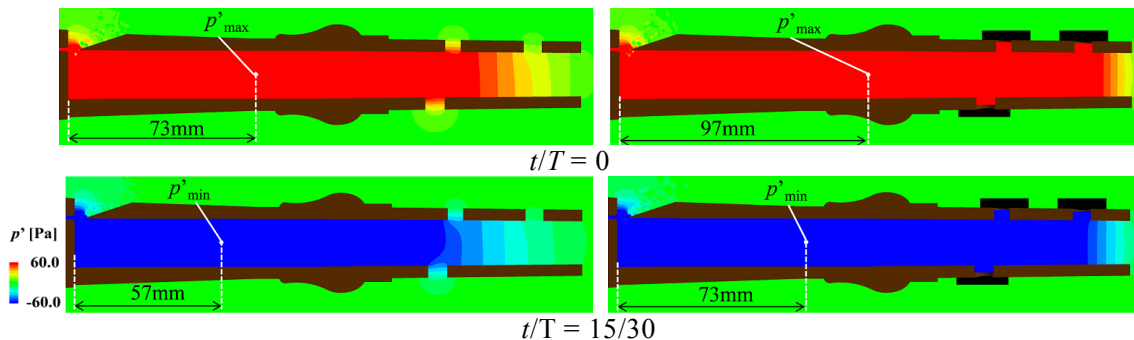


Figure 15 Fluctuation pressure for opened and closed tone holes.

To evaluate the open-end correction of the actual shape recorder, the path of the standing wave is examined base on Figure 15 and modeled as shown Figure 16. The path is changed with the state of tone holes. In order to quantitative evaluation of the path of the standing wave, phase difference of the sound pressure in the resonator are calculated by numerical results as shown in Figure 17, where the reference point of the phase difference is set at the antinode.

When the region of the standing wave determines within  $|\Delta\phi / 2\pi| \leq 0.12$ , the length of this region is in good agreement with half wavelength of the resonant frequency of the recorder. For opened tone holes, the open-end correction of the window is 30 mm and that of the resonator outlet is 21mm. For the closed tone holes, while 31 mm and 37mm. The discrepancies of these results and predicted values of conventional open-end correction are very large. It indicates that the conventional open-end correction model cannot apply to the acoustic field of the actual shape recorder which has very complicated shapes and acoustic field with uniform flow.

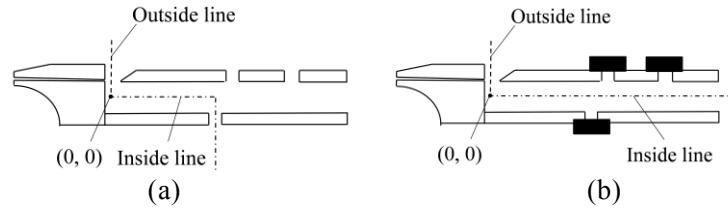


Figure 16 Path of standing wave in recorder. (a) With closed tone holes. (b) With opened tone holes

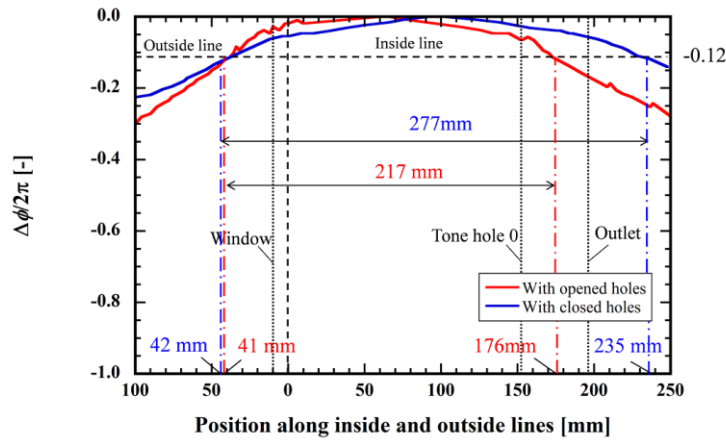


Figure 17 Phase difference of fluctuation pressure (close and open holes).

**4.2.2 Effects of Jet Velocity**

Figure 18 shows the phase difference of the pressure fluctuation for  $U_{max} = 11.3, 13.7$  m/s with opened tone holes. The open-end corrections of both sides become large at lower velocity of 11.3m/s. The result shows the jet velocity affect to the open-end correction of the recorder.

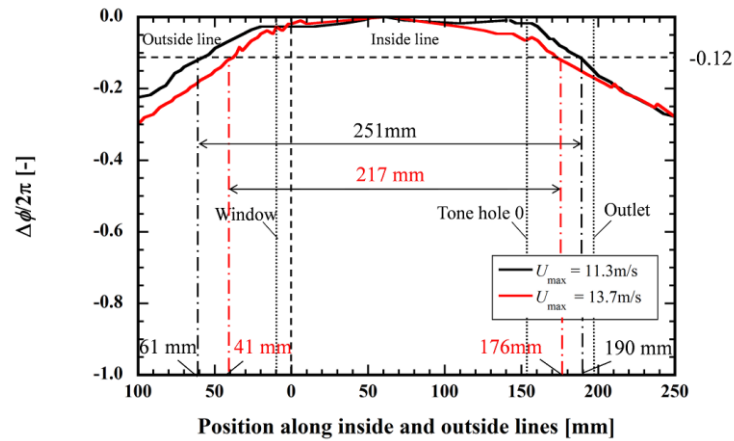


Figure 18 Phase difference of fluctuation pressure ( $U_{max} = 11.3, 13.7$  m/s).

## 5. CONCLUSIONS

In order to clarify generation mechanism of air-reed music instruments, interaction between the flow and acoustic fields are numerically investigated. The direct aeroacoustic simulations for an actual recorder were performed with three dimensional compressible Navier-Stokes equations.

The vorticity of vortex in free shear layer decreases near the edge, here, the vortices are deformed and expansion wave occurs in the resonator. The shear layers are receptive to the sound. Therefore, the oscillations of shear layers are synchronized with acoustic field of the resonator. And then the vortex shedding is also synchronized and sound level increases. The numerical results visualize sound receptivity of the shear layers. In the resonator, the amplitude and phase of acoustic particle velocity and those of fluctuation velocity of shear layer are almost the same. The direction of the shear layer oscillation corresponds to the direction of acoustic particle velocity. The path of the standing wave is modeled and quantitatively estimated by the phase difference of the sound pressure. The result shows the path is changed by the state of the tone holes. Moreover, the open-end corrections of actual recorder become quite large because of the influence the complicated shapes and velocity of the flow field. The node points of windway side are independent of conditions of tone holes. On the other hand, the node points of tone holes side are shifted increasing the wavelength. The maximum velocity of the jet affects the node points both sides of tone holes and windway.

## ACKNOWLEDGEMENTS

The present study was supported by JSPS KAKENHI Grant of No. 24760134, that of No. 26820044 and through the Next-generation Supercomputer Strategy Program by the Ministry of Education, Culture, Sports, Science, and Technology of Japan (MEXT).

## REFERENCES

- [1] Benoit F, Joël G, Avraham H, Xavier P. Aeroacoustics of Musical Instruments. *Annual Review of Fluid Mechanics*. Vol.44; 2011. p. 1-25.
- [2] Yoshikawa S, Tashiro H, Sakamoto Y. Experimental examination of vortex-sound generation in an organ pipe: A proposal of jet vortex-layer formation model. *Journal of Sound and Vibration*. Vol.331; 2012. p. 2558-2577.
- [3] Howe M. S. Contributions to the theory of aerodynamic sound, with application to excess jet noise and the theory of the flue. *Journal of Fluid Mechanics*. Vol.71; 1975. p. 625-673.
- [4] Giordano N. Simulation studies of a recorder in three dimensions. *The Journal of the Acoustical Society of America*, Vol. 135 (2); 2014. p. 906-916.
- [5] Lele S. K. Compact finite difference schemes with spectral-like resolution. *Journal of Computational Physics*. Vol.103; 1992. p. 16-19.
- [6] Liu O, Vasilyev O. V. A Brinkman penalization method for compressible flows in complex geometries. *Journal of Computational Physics*. Vol.227; 2007. p. 946-966.
- [7] Matsuura K, Kato C. Large-eddy simulation of Compressible Transitional Flows in a Low-Pressure Turbine Cascade. *AIAA Journal*, Vol.45; 2007. p. 442-457.
- [8] Gaitonde D. V, Visbal M. R. Pade-Type Higher-Order Boundary Filters for the Navier-Stokes Equations. *AIAA Journal*, Vol.38; 2000. p. 2103-2112.